(Received 20 January 2026, Accepted 5 March 2026, Scheduled 24 March 2026)

Design of Dual-Band Class F^{-1} Power Amplifier Based on the Integration of Harmonic Control and Fundamental Matching

Wen Huang[1,*], Junhao Zhao[2], Jiang Liu[1], and Honggang Hao[1]

[1] School of Electronic Science and Engineering, Chongqing University of Posts and Telecommunications, Chongqing 400065, China
[2] School of Integrated Circuits, Chongqing University of Posts and Telecommunications, Chongqing 400065, China

ABSTRACT: This paper proposes a dual-band class F^{-1} high-efficiency power amplifier with an integrated structure for harmonic suppression and fundamental matching. The fundamental matching network employed a dual-frequency coupler with open branches. This structure is partially reused for third-harmonic control by leveraging two open branches and two branch lines. By adjusting the characteristic impedance of the quarter-wavelength transmission line, the third-harmonic impedance is adjusted to a short circuit at both fundamental frequencies at the drain of the power amplifier. The second-harmonic control network consists of a quarter-wavelength open stub and a drain bias line loaded with a double-spiral defected ground structure (DGS), which controls the second-harmonic impedance to an open circuit state at the drain, satisfying the class F^{-1} harmonic conditions. A dual-band high-efficiency class F^{-1} power amplifier operating at 2.6 GHz/3.4 GHz is designed and fabricated. The measured results show drain efficiencies of 73.5% and 74.3% at 2.6 GHz/3.4 GHz, with output power exceeding 40 dBm and gain above 10 dB.

1. INTRODUCTION

With the rapid development of wireless communication, the demand for reduced power consumption in the entire system has become increasingly stringent. As a core component, the power efficiency of an radio frequency (RF) power amplifier (PA) directly affects the lifespan of the system. While high-efficiency PAs, such as class E, F, and F^{-1} offer theoretical efficiencies approaching 100%, they suffer from narrow bandwidths [1–3]. The design concept of a class J power amplifier was introduced by Cripps et al. in 2009 [4]. According to [4], the class J PA features an extensive impedance space that transcends open/short circuit limitations, enabling easier broadband design with a theoretical efficiency of 78.5%. Nevertheless, class F and F^{-1} remain the focus of research because of their high efficiency.

Defected ground structure (DGS) introduces equivalent reactive components by modifying the ground plane, creating specific stopbands to suppress spurious and higher-order modes. This significantly improves frequency selectivity [5]. Integrating DGS into power amplifier designs effectively suppresses harmonic interference, optimizes impedance matching, facilitates miniaturization, and enhances operational stability and energy efficiency [6].

Simultaneously, with the rapid development of 5G communication technology, PAs must operate in the 5G frequency band with a high efficiency. To address these challenges, this paper introduces an innovative co-design methodology for simultaneous harmonic control and fundamental matching. The approach integrates even and odd mode analysis of couplers with insights into harmonic control and bias circuit fusion from reference [7]. Notably, the second-harmonic control network incorporates a compact drain bias line loaded with a novel double-spiral DGS and a quarter-wavelength open stub, achieving an open circuit condition at the second harmonic without occupying extra area. Moreover, the third-harmonic control network is intelligently merged with the fundamental matching network, significantly simplifying the overall circuit architecture. To validate the theoretical feasibility, a dual-frequency high-efficiency class F^{-1} PA operating at 2.6 GHz and 3.4 GHz is designed and fabricated. The measured results demonstrate that the maximum drain efficiencies are 73.5% and 74.3% at the respective frequencies, with an output power exceeding 40 dBm and a gain above 10 dB.

* Corresponding author: Wen Huang (huangwen@cqupt.edu.cn).

2. THEORETICAL ANALYSIS

2.1. Theoretical Analysis of Class F^{-1} Power Amplifiers

Class F^{-1} PAs achieve a high efficiency by controlling the drain voltage and current waveforms. Specifically, the drain current is manipulated into a square wave, whereas the drain voltage is approximated as a half-sine wave. This ensures that the voltage and current waveforms barely overlap, thereby achieving an ideal efficiency of 100% [8, 9]. The corresponding mathematical expressions for the voltage and current are as follows:

$$V_1 = \frac{\pi}{2} V_{dc} \tag{1}$$

$$I_1 = \frac{4 I_{dc}}{\pi} \tag{2}$$

where V_{DC} and I_{DC} are the DC voltage and current, respectively. For an ideal class F^{-1} PA, where the drain voltage is

a perfect sine wave, and the drain current is an ideal square wave with no overlap, the expressions for the fundamental output power P_1 and DC power P_{dc} are given by:

$$P_1 = P_{dc} = V_{dc} I_{dc} \tag{3}$$

Theoretically, the drain efficiency of a class F^{-1} PA can be expressed by

$$\eta_{DE} = \frac{P_1}{P_{dc}} = 100\% \tag{4}$$

Controlling harmonics in class F^{-1} PAs is challenging because of the presence of parasitic parameters within the transistor. Typically, only up to the third harmonic is controlled, because higher harmonics are difficult to control. The conditions for achieving the ideal efficiency of 100% in class F^{-1} PA are as follows:

$$Z_{f_0} = R_{f_0} = \pi^2 \frac{V_{dc}}{8 I_{dc}} \tag{5}$$

$$Z_{2f_0} = \infty \tag{6}$$

$$Z_{3f_0} = 0 \tag{7}$$

where Z_{f_0} represents the fundamental impedance, Z_{2f_0} the second harmonic impedance, and Z_{3f_0} the third harmonic impedance. It indicates that the second-harmonic impedance is infinite, corresponding to an open circuit condition; the third-harmonic impedance is zero, corresponding to a short circuit condition, the efficiency of the class F^{-1} PA can reach a theoretical value of 100%.

2.2. Theoretical Analysis of Dual-Frequency Fundamental Matching Networks

Based on the load-pull and source-pull simulations by the advanced design system (ADS) software, the load impedances at $f_1 = 2.6$ GHz and $f_2 = 3.4$ GHz are determined as $(14.767 + \text{j}12.186)\ \Omega$ and $(15.709 + \text{j}1.476)\ \Omega$, respectively. Using these values, the fundamental load matching network is designed to achieve optimal PA performance at both frequencies. The proposed dual-frequency fundamental load matching network is illustrated in Fig. 1.

Based on the theoretical analysis of the microstrip coupler in [10], the dual-band fundamental impedance matching network consists of four T-branches with open stubs. To better illustrate the design process, the subsequent analysis focuses on

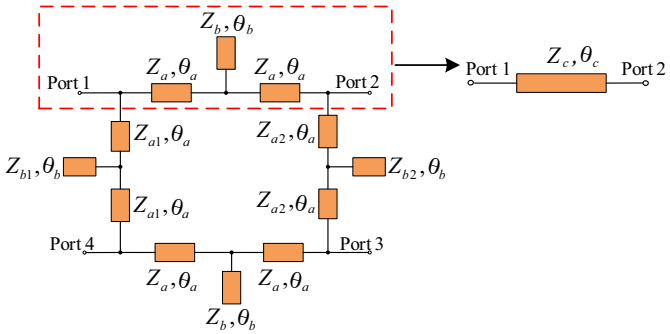

FIGURE 1. Dual-frequency fundamental load impedance matching network.

the individual T-shaped branch section, as indicated by the red box in Fig. 1. This structure consists of three cascaded subnetworks: a left series segment, a parallel stub, and a right series segment. Its overall $ABCD$ matrix is given by:

$$\begin{bmatrix} A_T & B_T \\ C_T & D_T \end{bmatrix} = \begin{bmatrix} \cos\theta_a & jZ_a \sin\theta_a \\ \frac{j\sin\theta_a}{Z_a} & \cos\theta_a \end{bmatrix} \times \begin{bmatrix} 1 & 0 \\ \frac{j\tan\theta_b}{Z_b} & 1 \end{bmatrix} \times \begin{bmatrix} \cos\theta_a & jZ_a \sin\theta_a \\ \frac{j\sin\theta_a}{Z_a} & \cos\theta_a \end{bmatrix} \tag{8}$$

Because this structure is equivalent to a conventional quarter-wavelength transmission line, its $ABCD$ matrix is identical to that of the conventional quarter-wavelength transmission line.

$$\begin{bmatrix} A_T & B_T \\ C_T & D_T \end{bmatrix} = \begin{bmatrix} 0 & \pm jZ_c \\ \pm j\frac{1}{Z_c} & 0 \end{bmatrix} \tag{9}$$

where Z_c is the characteristic impedance of a conventional quarter-wavelength line. Setting $A_T = D_T = 0$ yields:

$$\tan\theta_b = \frac{Z_b(\cos^2\theta_a - \sin^2\theta_a)}{Z_a \sin\theta_a \cos\theta_a} \tag{10}$$

$$B_T = jZ_a \tan\theta_a \tag{11}$$

$$C_T = j\frac{1}{Z_a \tan\theta_a} \tag{12}$$

Therefore, the $ABCD$ matrix of the T-branch is simplified to:

$$\begin{bmatrix} 0 & jZ_a \tan\theta_a \\ j\frac{1}{Z_a \tan\theta_a} & 0 \end{bmatrix} = \begin{bmatrix} 0 & \pm jZ_c \\ \pm j\frac{1}{Z_c} & 0 \end{bmatrix} \tag{13}$$

For dual-band operation, the necessary conditions are:

$$Z_a \tan\theta_{af_1} = \pm Z_c \tag{14}$$

$$Z_a \tan\theta_{af_2} = \pm Z_c \tag{15}$$

where θ_{af1} and θ_{af2} are the electrical lengths of the lines at frequencies f_1 and frequency $f_2 (\theta_{af1} < \theta_{af2})$.

The solution of (14) and (15) is:

$$\theta_{af_1} + \theta_{af_2} = n\pi \tag{16}$$

where $n = 1, 2, 3, \ldots$, and the electrical length of transmission lines is:

$$\theta = \frac{2\pi f L}{c\sqrt{\varepsilon_r}} \tag{17}$$

Here, L is the physical length, c the speed of light, and ε_r the dielectric constant of the substrate. The electrical length is therefore proportional to the frequency:

$$\frac{\theta_{f1}}{\theta_{f2}} = \frac{f_1}{f_2} \tag{18}$$

It can be deduced that:

$$\theta_{af_0} = n\pi \tag{19}$$

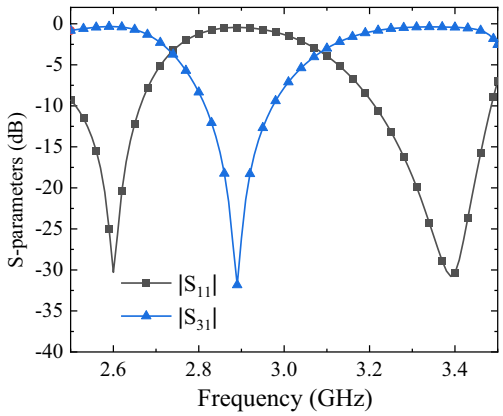

FIGURE 2. S-parameter simulations of the proposed dual-band fundamental loading impedance matching network.

where $f_0 = f_2 \pm f_1$ and $\theta_{af0} = \theta_{af2} \pm \theta_{af1}$. Consequently, once the two operating frequencies are determined, the electrical lengths of the series section at these two frequencies (θ_{af1} and θ_{af2}) are also determined. Combining (10) and (16) yields:

$$\tan\theta_{bf1} = \pm\tan\theta_{bf2} \tag{20}$$

where θ_{bf1} and θ_{bf2} are the electrical lengths of shunt section θ_b at the two frequencies.

Therefore, (20) leads to:

$$\theta_{bf_0} = m\pi \tag{21}$$

where $m = 1, 2, 3, \ldots$. Using (18), (19), and (21), the values of θ_{af1}, θ_{af2}, θ_{bf1}, and θ_{bf2} at two operating frequencies (2.6 GHz/3.4 GHz) are calculated with $m = 1$ and $n = 1$ for simplicity. Furthermore, Z_A and Z_B are obtained using (14) and (10), respectively. The impedance parameters of each line are derived from the formula and optimized through ADS software simulation, and their characteristic impedance and electrical length are shown in Table 1. These values ensure that the real part of the load impedance matches a port impedance of 50 Ω. When ports 4 and 2 are open circuit, simulations are performed to obtain the performance results of the dual-frequency fundamental load impedance network structure, which are presented in Fig. 2.

TABLE 1. Characteristic impedance and electrical length of dual-band harmonic control network.

Parameter	Z_a	Z_b	Z_{a1}	Z_{b1}	Z_{a2}	Z_{b2}
Characteristic impedance (Ω)	20.7	43.9	16.6	45.2	45.3	94.6
Electrical lengths (°)	14.8	7.9	13	5.5	15	14.8

It is evident from Fig. 2 that at frequencies of 2.6 GHz and 3.4 GHz, $|S_{11}|$ is below −20 dB, while $|S_{31}|$ approaches 0 dB. Consequently, the simulation results demonstrate that the dual-band matching network exhibits excellent fundamental load impedance matching performance at the frequencies of 2.6 GHz and 3.4 GHz. Because the load impedance is a complex, it is necessary to load a high-impedance transmission line at the input port of the dual-band fundamental load impedance matching network during the subsequent design. This enables the load impedance to match the 50 Ω port impedance, which ensures that the load impedance is matched to the standard 50 Ω port impedance.

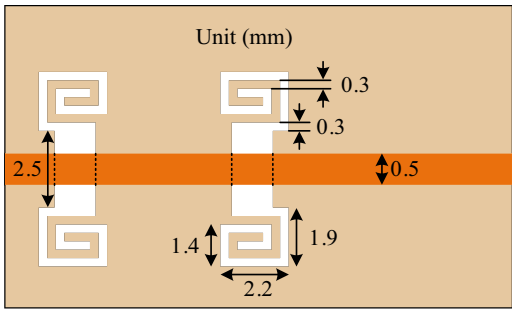

FIGURE 3. The drain bias line loaded with double spiral DGS.

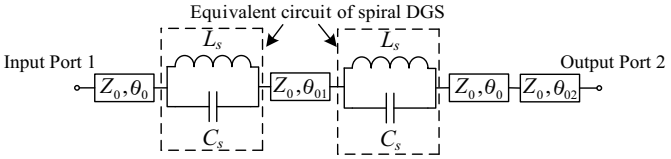

FIGURE 4. Equivalent circuit of a drain bias lines with a double-spiral DGS.

To visually illustrate the design approach for dual-frequency matching networks, the simplified process is as follows:

1. Using (18), (19), and (21), the values of θ_{af1}, θ_{af2}, θ_{bf1} and θ_{bf2} are obtained at the two operating frequencies, where the value of n and m are set to 1 for compactness.
2. Using (14) and the designated characteristic impedance Z_c, the value of Z_A is calculated.
3. The value of Z_B is calculated using (10) combined with the parameters obtained in the previous two steps.
4. The physical lengths of the two stubs are determined for the different characteristic impedances Z_A and Z_B.

2.3. Theoretical Analysis of Dual-Frequency Harmonic Control Networks

Based on the theoretical analysis of class F^{-1} PA, the drain harmonic control conditions require an open circuit at the second harmonic and a short circuit at the third harmonic. The core of this dual-frequency harmonic control network design is to share part of the third-harmonic control structure with the fundamental matching network. The second harmonic control network is implemented using a drain bias line loaded with a double-spiral DGS and an open circuit transmission line, with the specific parameters shown in Fig. 3. Fig. 4 illustrates the equivalent circuit of the DGS loaded bias line, which comprises two cascaded parallel resonant circuits. A detailed theoretical analysis of this structure for controlling harmonic impedance is provided in [5]. The overall structure of the dual-frequency harmonic control network is shown in Fig. 5.

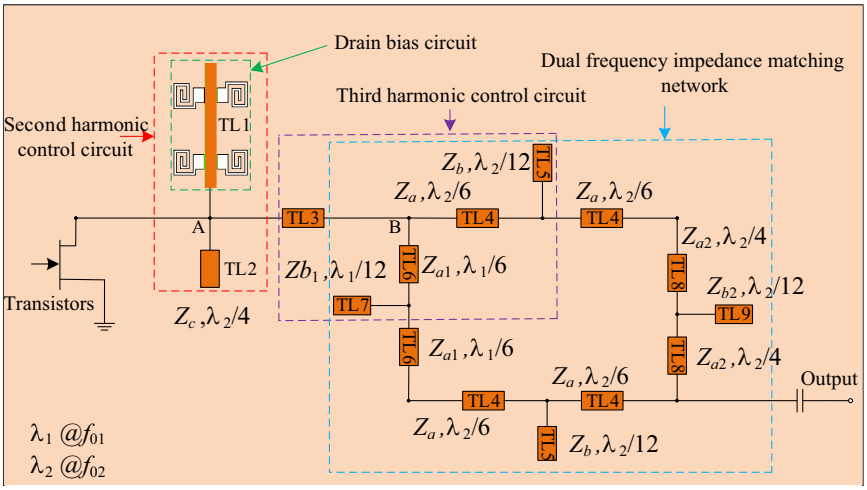

FIGURE 5. Dual-band harmonic control network.

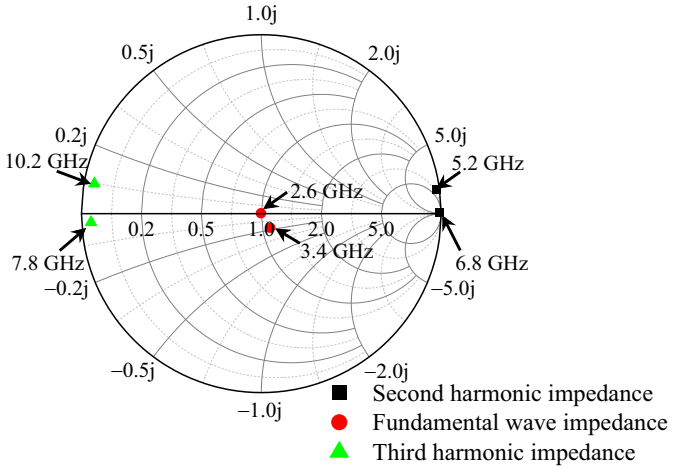

FIGURE 6. The variation of fundamental and harmonic impedance trajectory in the harmonic control network at the drain ends.

The second-order harmonic control network depicted in Fig. 5 primarily consists of a drain bias line loaded with a double-spiral DGS and quarter-wavelength open circuit stub TL2 at $f_{02} = 3.4$ GHz. Consequently, a properly dimensioned double-spiral DGS tunes the second-order harmonic impedance at $2f_{01} = 5.2$ GHz to near open circuit. The quarter-wavelength open circuit stub TL2 at $f_{02} = 3.4$ GHz, for the second-harmonic frequency $2f_{02}$, acts as a half-wavelength stub. Therefore, for the second-harmonic frequency at $2f_{02} = 6.8$ GHz, the open circuit condition is converted to an open circuit at point A. Thus, at point A, the second-harmonic impedance at both $2f_{01} = 5.2$ GHz and $2f_{02} = 6.8$ GHz is effectively controlled near the open circuit point.

The third-harmonic control network primarily consists of transmission line TL3 with an electrical length of 60° at f_{01} and transmission lines TL4, TL5, TL6, and TL7. At the third harmonic frequency $3f_{01}$ (7.8 GHz), transmission line TL3 of length $\lambda/6$ at f_{01} is equivalent to a half-wavelength length at $3f_{01}$, and the impedance at point A is the same as that at point B.

At the third harmonic at $3f_{02}$ (10.2 GHz), TL5 with a one-twelfth wavelength length at f_{02} is equivalent to a quarter-wavelength length, and TL4 with a one-sixth wavelength length at f_{02} is equivalent to a half-wavelength length. Similarly, at the third harmonic at $3f_{01}$ (7.8 GHz), TL7 with a one-twelfth wavelength length at f_{01} acts as a quarter-wavelength length, and TL6 with a one-sixth wavelength length at f_{01} acts as a half-wavelength length. Consequently, after transformation by TL4-TL5 and TL6-TL7, the third harmonic impedances at both $3f_{02}$ and $3f_{01}$ are positioned near the short circuit point at B. Because TL3 preserves this impedance from B to A, the third harmonic at A is also near the short circuit. Because TL3 preserves this impedance from B to A, the third harmonic at A is near the short circuit. Thus, the second and third harmonic impedances at point A satisfy the class F^{-1} requirement. The impedance trajectories after the simulation optimization are shown in Fig. 6.

The Smith chart confirms that the fundamental impedance is located near the center, indicating a good match between the optimal load impedances and the port impedance at both fundamental frequencies. Furthermore, the second and third harmonic impedances are positioned close to the open and short circuit points, respectively. This confirms that the drain harmonic impedances are effectively controlled and satisfy the class F^{-1} requirements, which is expected to enhance the drain efficiency of the PA.

2.4. Overall Simulation of Power Amplifier

To validate the theoretical feasibility, the proposed PA is simulated using a Rogers 4350B substrate ($\varepsilon_r = 3.66$, $h = 0.508$ mm) and a Cree CGH40010F GaN HEMT biased at $V_{GS} = -2.7$ V and $V_{DS} = 28$ V. The overall structure is depicted in Fig. 7, where the light orange color indicates the presence of grounding plate metal on the back, while the orange sections represent the metal microstrip line on the front. Input harmonic control is omitted because of its minimal impact on performance. A small-signal RC stabilization network (7 pF Murata capacitor, 8 Ω 0805 resistor) is added at the input to prevent self-oscillation.

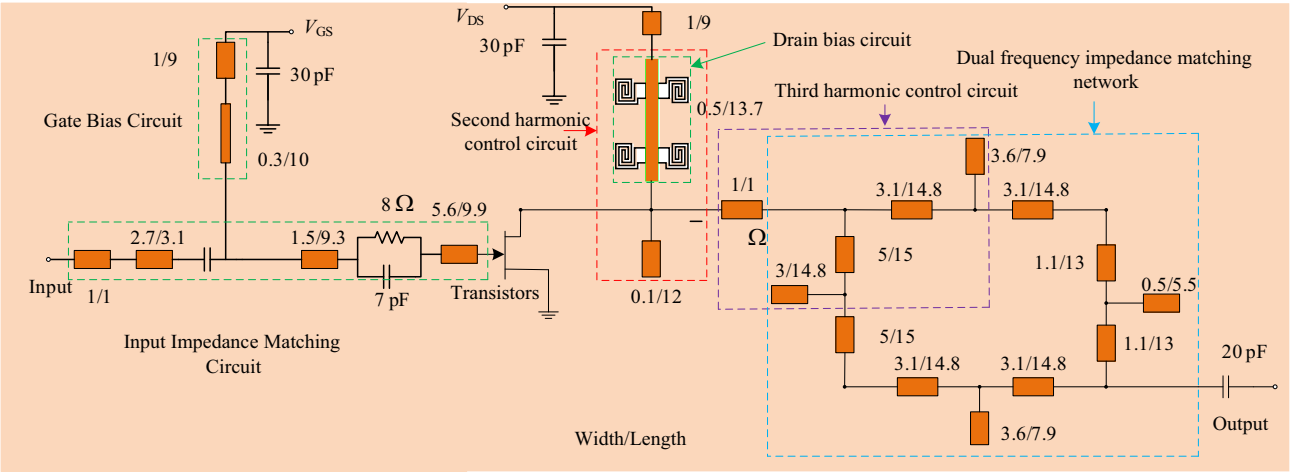

FIGURE 7. Overall schematic of the proposed PA.

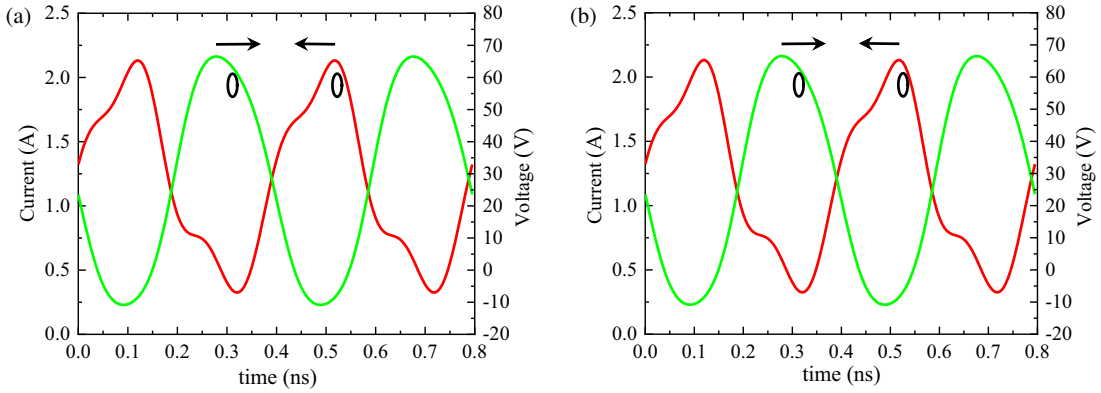

FIGURE 8. The drain voltage and current waveforms of the PA at two different frequencies. Minimal overlap between the two waveforms confirms the desired class F^{-1} waveform shaping.

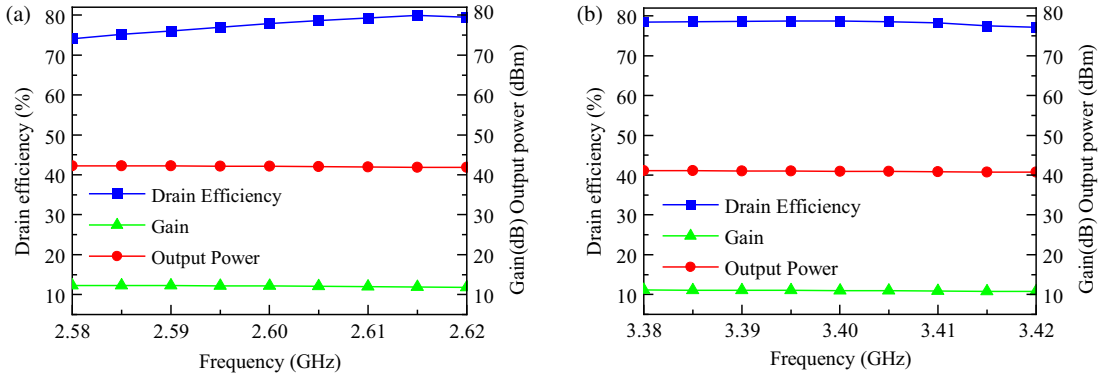

FIGURE 9. Simulated efficiency, output power and gain curves at two frequencies.

Figure 8 shows the drain voltage and current waveforms at both fundamental frequencies under a large-signal ADS simulation. The minimal overlap between the waveforms confirms good agreement with the class F^{-1} characteristics, satisfying the requirements for high efficiency.

Using a single-tone continuous wave input, the PA reached saturation at an input power of 28 dBm after simulation optimization. As shown in Fig. 9, the simulated drain efficiency is 79.9% and 78.7% at 2.6 GHz and 3.4 GHz, respectively, with output power $>$ 40 dBm and gain $>$ 10 dB at both frequencies, basically meeting the design specifications.

A photograph of the fabricated PA is shown in Fig. 10, and its measured performance is shown in Fig. 11. The measured drain efficiency is 73.5% and 74.3% at 2.6 GHz and 3.4 GHz, respectively, and remains above 70% within 20 MHz of each center frequency. It indicates that DC energy has been efficiently con-

TABLE 2. Comparison of the proposed power amplifier with reported typical dual-band power amplifier.

Ref.	class	Tech.	Frequency (GHz)	Output Power (dBm)	Drain Efficiency (%)	Gain (dB)
[11]	F	GaN	2.2/2.6	39.8/40.03	72.5/67.8	> 10
[12]	J	GaN	1.7/2.6	41/41	70/64	11/11
[13]	F	GaN	1.4/2.4	41/40	65/67	13/12.5
[14]	J	GaN	2.35/3.45	40.6/41.2	70.3/71.4	10.6/11.2
[15]	F	GaN	2.6/3.4	39.8/39.5	64/62	11/10.8
This	F^{-1}	GaN	2.6/3.4	40.6/40.8	73.5/74.3	10.6/10.8

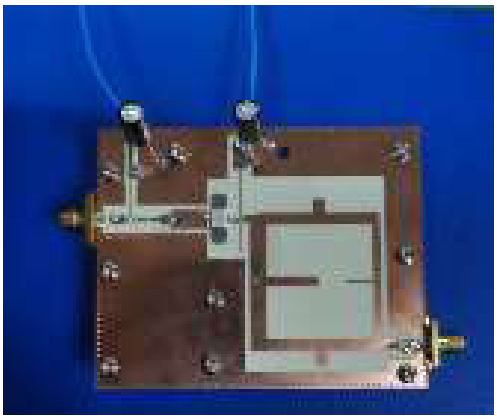

FIGURE 10. Photo of the fabricated power amplifier.

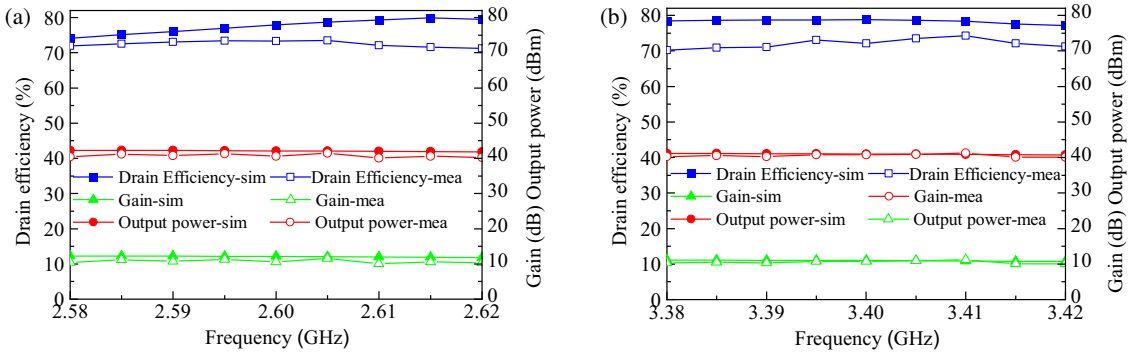

FIGURE 11. Simulations and measurements of drain efficiency, output power, and gain.

verted into the fundamental frequency output, directly reflecting the excellent harmonic control performance. The output power exceeds 40 dBm, and the gain is greater than 10 dB at both frequencies. The measured large-signal performance is slightly degraded compared to the simulation, mainly owing to welding, heat dissipation, and other practical factors. Table 2 compares the performance of the proposed PA with recent domestic and international designs, showing good performance such as high efficiency.

3. CONCLUSIONS

In this study, a high-efficiency dual-frequency class F^{-1} PA with an integrated design of harmonic control and fundamental matching is proposed. A drain bias line loaded with a double-spiral DGS with a quarter-wavelength open circuit stub is used to present an open circuit state at the second harmonic. The impedance-transforming branch-line coupler serves as a dual-frequency fundamental matching network, and a portion of this coupler is utilized to control the third-harmonic impedance for a short-circuit state. The measured results confirm the effectiveness and feasibility of the proposed design approach for the harmonic control circuit of the PA.

ACKNOWLEDGEMENT

This work was supported by the Scientific and Technological Research Program of the Chongqing Municipal Education Commission (KJQN202300611), the Chongqing Natu-

ral Science Foundation General Program (CSTB2025NSCQ-GPX1291), and the Chongqing Postgraduate Research and Innovation Project (CYS240430).

REFERENCES

[1] Tahmasbi, M., F. Razaghian, and S. Roshani, "Design of high-efficiency Hybrid Power Amplifier with concurrent F&F^{-1} class operations for 5G application," *Frequenz*, Vol. 75, No. 11–12, 467–477, 2021.

[2] Xuan, X., Y. Liu, M. Zhai, Y. Wang, X. Ge, G. Liu, and Z. Cheng, "Design of bandwidth-enhanced power amplifier based on class-EF modes," *Microwave and Optical Technology Letters*, Vol. 63, No. 8, 2122–2128, 2021.

[3] Feng, W., W. Wu, X. Y. Zhou, W. Che, and Y. Shi, "Broadband high-efficiency quasi-class-J power amplifier based on nonlinear output capacitance effect," *IEEE Transactions on Circuits and Systems II: Express Briefs*, Vol. 69, No. 4, 2091–2095, 2022.

[4] Cripps, S. C., P. J. Tasker, A. L. Clarke, J. Lees, and J. Benedikt, "On the continuity of high efficiency modes in linear RF power amplifiers," *IEEE Microwave and Wireless Components Letters*, Vol. 19, No. 10, 665–667, 2009.

[5] Faeghi, P. and J. S. Walling, "A probe antenna with an integrated band-pass filter via shielded SIW," in *2025 IEEE Texas Symposium on Wireless and Microwave Circuits and Systems (WMCS)*, 1–4, Waco, TX, USA, 2025.

[6] Lim, J.-S., H.-S. Kim, J.-S. Park, D. Ahn, and S. Nam, "A power amplifier with efficiency improved using defected ground structure," *IEEE Microwave and Wireless Components Letters*, Vol. 11, No. 4, 170–172, 2001.

[7] Huang, W. and J. Liu, "High-efficiency class-F power amplifier based on double spiral defected ground structure," *International Journal of Electronics*, Vol. 111, No. 3, 485–498, 2024.

[8] Kazimierczuk, M. K., *RF Power Amplifiers*, John Wiley & Sons, 2014.

[9] Woo, Y. Y., Y. Yang, and B. Kim, "Analysis and experiments for high-efficiency class-F and inverse class-F power amplifiers," *IEEE Transactions on Microwave Theory and Techniques*, Vol. 54, No. 5, 1969–1974, 2006.

[10] Zhang, H. and K. J. Chen, "A stub tapped branch-line coupler for dual-band operations," *IEEE Microwave and Wireless Components Letters*, Vol. 17, No. 2, 106–108, 2007.

[11] Gao, M., G. Xu, and J. Nan, "Design of concurrent tri-band high-efficiency power amplifier based on wireless applications," *Electronics*, Vol. 11, No. 21, 3544, 2022.

[12] Chen, P., S. He, X. Wang, and Z. Dai, "1.7/2.6 GHz high-efficiency concurrent dual-band power amplifier with dual-band harmonic wave controlled transformer," *Electronics Letters*, Vol. 50, No. 3, 184–185, 2014.

[13] Meng, X., C. Yu, Y. Wu, and Y. Liu, "Design of dual-band high-efficiency power amplifiers based on compact broadband matching networks," *IEEE Microwave and Wireless Components Letters*, Vol. 28, No. 2, 162–164, 2018.

[14] Dai, Z., S. He, J. Pang, J. Peng, C. Huang, and F. You, "Sub-optimal matching method for dual-band class-J power amplifier using real frequency technique," *IET Microwaves, Antennas & Propagation*, Vol. 11, No. 9, 1218–1226, 2017.

[15] Chen, H., G.-X. Liu, F. Zhu, M.-T. Han, and D. Jiang, "Design of dual-band power amplifier based on tri-band impedance matching circuit," *Journal of Electromagnetic Waves and Applications*, Vol. 35, No. 12, 1601–1610, 2021.